Research article

Plant-based calcium silicate from rice husk ash: A green adsorbent for free fatty acid recovery from waste frying oil

Zainor Syahira Zainal [a], Pengyong Hoo [a,b,*], Abdul Latif Ahmad [c], Ahmad Zuhairi Abdullah [c], Qihwa Ng [a,b], Siewhoong Shuit [d], Siti Kartini Enche Ab Rahim [a,b], Jeyashelly Andas [e]

[a] *Faculty of Chemical Engineering & Technology, Universiti Malaysia Perlis, 02600 Arau, Perlis, Malaysia*
[b] *Centre of Excellence for Frontier Materials Research (CFMR), Universiti Malaysia Perlis, 02600 Arau, Perlis, Malaysia*
[c] *School of Chemical Engineering, Engineering Campus, Universiti Sains Malaysia, 14300 Nibong Tebal, Penang, Malaysia*
[d] *Department of Chemical Engineering, Lee Kong Chian Faculty of Engineering & Science, Universiti Tunku Abdul Rahman, Sungai Long Campus, Jalan Sungai Long, Bandar Sungai Long, Cheras, 43000, Kajang, Selangor, Malaysia*
[e] *Faculty of Applied Sciences, Universiti Teknologi MARA, Cawangan Perlis, Campus Arau, 02600, Perlis, Malaysia*

ABSTRACT

Driven by the urgent need for a solution to tackle the surge of rice husk (RH) and waste frying oil (WFO) waste accumulation at a global scale, this report highlights the use of calcium silicates (CS) extracted from acid-pre-treated rice husk ash (RHA) for free fatty acid (FFA) removal from WFO as conventional RHA shows limited FFA adsorption performance. A novel alkaline earth silicate extraction method from acid-pre-treated RHA was outlined. The structural and behavioural attributes of the synthesised CS were identified through BET, SEM-EDS, and XRD analyses and compared to those of RHA. Notable morphology and structural modification were determined, including reducing specific surface areas, mitigating from amorphous to crystalline structure with regular geometric forms, and detecting Si–O–Ca functional groups exclusive to CS adsorbents. A comparison study showed superior lauric acid (LA) adsorption performance by CS absorbents over acid-pre-treated RHA, with a significant increase from 0.0831 ± 0.0004 mmol LA/g to 2.5808 ± 0.0011 mmol LA/g after 60 min. Recognised as the best-performing CS adsorbent, CS-1.0 was used for further investigations on the effect of dosage, LA concentration, and temperature for efficient LA adsorption, with up to 100% LA removal and 5.6712 ± 0.0016 mmol LA/g adsorption capacity. The adsorption isotherm and kinetic studies showed LA adsorption onto CS-1.0 followed Freundlich isotherm with $K_F = 0.0598$ mmol$^{(1-1/n)}$ L$^{(1/n)}$ g^{-1} & $Q_{e,cal} = 3.1696$ mmol g^{-1} and intraparticle diffusion model with $k_{id} = 0.1250$ mmol g^{-1} min$^{0.5}$ & $C_i = 0.9625$ mmol g^{-1}, indicating rapid initial adsorption and involvement of carboxylate end of LA and the calcium ions on the CS-1.0 in the rate-limiting step. The high equilibrium adsorption capacity and LA adsorption rate indicated that the proposed CS-1.0 adsorbent has excellent potential to recover FFA from WFO effectively.

* Corresponding author. Faculty of Chemical Engineering & Technology, Universiti Malaysia Perlis, 02600 Arau, Perlis, Malaysia.
E-mail address: pengyong@unimap.edu.my (P. Hoo).

1. Introduction

The multifaceted properties of rice husk (RH) have garnered substantial research attention in recent years, positioning it as a versatile resource for diverse applications. RH, a by-product of paddy grain milling, exhibits a composition rich in hemicellulose (14.04–29.3 %), cellulose (28.6–41.52 %), and lignin (12.84–33.67 %) [1]. The surge in rice production due to global population growth intensifies RH waste accumulation, necessitating effective waste management strategies. Leveraging its sustainability and cost-effectiveness, RH finds second-life applications in renewable energy storage, soil enhancement, and beyond [2,3].

A significant subset of research has also concentrated on rice husk ash (RHA), a by-product obtained through RH calcination [3]. RH and RHA notably display exceptional adsorption capabilities attributed to their porous structures [4,5]. However, their adsorption performances differ due to varying composition and silica contents, which are significantly influenced by calcination parameters and the composition of RH itself [6]. RHA's exceptional adsorption potential has been harnessed for various pollutants in wastewater, including heavy metals and dyes. Additionally, RHA's efficacy in adsorbing free fatty acids (FFAs) from waste frying oil (WFO) has emerged as a promising solution for a challenging environmental issue stemming from its ecotoxic nature and potential to contaminate soil and water sources [7].

While most attention has centred on optimising adsorption methodologies using RH and RHA in tackling the aforementioned challenge, in this study, the augmentation of adsorption efficiency through the extraction of alkaline earth silicates from acid-pre-treated RHA is delved, with a specific focus on enhancing the removal of FFAs from WFO as literature reports indicated rooms for improvement [7,8]. Subjecting to either inorganic or organic acids such as acetic acid (CH_3COOH), sulfuric acid (H_2SO_4), and hydrochloric acid (HCl) before combustion, conventional acid pre-treatment of RH initiates hydrolysis and decomposition of organic components, along with leaching of soluble metal impurities such as magnesium (Mg) and manganese (Mn) [9,10]. The treatment increases silica purity post-calcination, resulting in a higher specific surface area by enlarging the existing pores and creating new ones, thereby enhancing accessible adsorption sites on the RHA surface [11].

However, acid-pre-treated RHA showed low FFA adsorption performance, attributed to the simultaneous oxidation and hydrolysation reactions during heating of the WFO catalysed by the minimal acid residue in the acids-pre-treated RHA [12]. This study explores the extraction and application of purified silicate extracted from RH using the novel alkaline earth precipitation method to achieve enhanced FFA adsorption. The resulting alkaline earth metal silicate precipitate could yield highly purified silicates that greatly benefit the study's adsorption. This study narrows its focus on calcium silicate derived from HCl pre-treated RH for enhanced adsorption of LA (one of the FFA constituents of WFO), owing to the limited attention paid to calcium silicate and its efficacy in FFA removal from WFO.

By exploring the structural attributes of calcium silicate and its adsorptive behaviours, this study aims to provide insights into its potential for efficient FFA adsorption, contributing to the advancement of sustainable wastewater treatment methodologies. Besides, understanding the adsorption kinetics and equilibrium is essential for adsorber design and commercialisation. Thus, various kinetic models (pseudo-first-order, pseudo-second-order, Elovich equation, intra-particle diffusion) were proposed and applied to determine LA's adsorption rate and mechanism onto calcium silicate. Langmuir, Freundlich, and Temkin adsorption isotherms were also employed to predict the maximum adsorption capacities and elucidate the nature of the studied adsorption, providing complimentary yet crucial information for further industrial application and commercialisation.

2. Materials and methods

2.1. Chemicals and materials

RH was sourced from Dibuk Sdn. Bhd., Kangar, Perlis. Calcium hydroxide, $Ca(OH)_2$ (EMSURE® ACS, ≥95% purity), sodium hydroxide, NaOH (EMSURE® ACS, ≥97% purity), hydrochloric acid, HCl (EMSURE® ACS, 37% purity), isooctane, $(CH_3)_3CCH_2CH(CH_3)_2$ (EMSURE® ACS, ≥99% purity), isopropyl alcohol, IPA (EMSURE® ACS, ≥99.9% purity) were purchased from Biotek Abadi (Butterworth, Penang, Malaysia). Lauric acid, $C_{12}H_{24}O_2$ (A.R. ≥ 98% purity), potassium bromide, KBr (A.R., ≥99.5% purity), and phenolphthalein, $C_{20}H_{14}O_4$ (RMstain, 1% alcoholic solution), were purchased from Kumpulan Saintifik F.E. Sdn. Bhd. (KSFE) (Petaling Jaya, Selangor, Malaysia). All chemicals and materials were used without further purification unless otherwise mentioned.

2.2. Pre-treatment of RH

The acid pre-treatment of the fresh RH was done using an HCl solution, as described in the literature [13]. 10 g of RH was refluxed at 50 °C in 50 mL of 3 M HCl for 3 h before being filtered and washed with distilled water until the pH of the effluent remained unchanged. The washed RH was dried in the oven at 100 °C for 12 h before being combusted at 500 °C for 2 h (ramping rate 10 °C/min) using a Thermo Scientific Moldatherm™ Box Furnaces. The burnt black powder obtained after the calcination process was termed RHA.

2.3. Synthesis of calcium silicates

RHA was ground and sieved to particle sizes below 100 μm using a mortar. Then, at 100 °C, 4.4g of RHA were refluxed with 100 mL of 15% NaOH solution under stirring for 120 min at 300 rpm. The mixture was then filtered to extract the SiO_3^{2-} leachate. The leachate was reacted with 70 mL of $Ca(OH)_2$ solution at 95 °C for 1 h with continuous stirring under reflux. The precipitate was filtered and

washed with deionised water before oven-drying at 100 °C for 12 h to obtain calcium silicate. The calcium silicate produced using 0.5 M Ca(OH)$_2$ solution was labelled as CS-0.5, while those synthesised using 1.0 M Ca(OH)$_2$ and 1.5 M Ca(OH)$_2$ solutions were termed CS-1.0 and CS-1.5, respectively.

2.4. Material characterisations

Brunauer-Emmett-Teller (BET) surface analysis was applied to observe the specific surface areas and porosimetry of both HCl pre-treated RHA and calcium silicates using an automatic surface area analyzer (ASAP 2020, Micromeritics, USA). All samples were degassed for 2 h under vacuum at 200 °C before performing the analysis at 77 K. The detection of functional groups was done via the KBR method using PerkinElmer Fourier transform infrared spectroscopy (FTIR) (Waltham, USA). KBr and the samples were dried at 110 °C for 12 h before 3 mg of samples were mixed and ground with 30 mg of KBr to form a pellet for subsequent measurements [14]. The pellet was scanned between 4000 and 400 cm^{-1} with ten scans and 4 cm^{-1} resolution. The surface morphology and composition of the samples were investigated using a scanning electron microscope coupled with energy-dispersive X-ray (SEM-EDX, JEOL, JSM-6460LA, Japan). All samples were deposited on a sample holder with a double-sided conducting carbon tape and coated with gold to improve the surface conductivity before performing the analysis using a 10 kV accelerating electron beam [15]. X-ray diffraction analysis (XRD, D2 Phaser, Bruker, US) was used to reveal the main crystalline phases of the samples, performed using Cu Kα radiation (λ = 1.5406 Å) at 40 kV and 45 mA, with a diffraction angle between 10 and 90° and a scanning rate of 0.5°/min [15]. Thermogravimetry analysis (TGA 7 Thermogravimetric Analyzer, PerkinElmer, USA) was done to identify the thermal stability and investigate the characteristic decomposition patterns of the studied materials. All materials were purged with nitrogen gas and heated from 30 to 900 °C at a ramping rate of 10 °C/min.

2.5. FFA stock solution preparation and IPA neutralisation

LA was used as the stock FFA throughout this study. To prepare 100 mmol/L of LA stock solution, 20.03 g of LA was dissolved in 1 L of isooctane. The solutions with the desired FFA concentrations (10, 20, 30, 40, and 50 mmol/L) were prepared by diluting the stock solution using Equation (1): $M_1 V_2 = M_2 V_2$ where M_1 and M_2 (mmol/L) represent the concentration of the stock solution and the desired solution, respectively, and V_1 and V_2 (L) denote the volume of the stock solution and the desired solution. 75 mL of IPA and 2 mL of phenolphthalein were added to a 100 ml conical flask to neutralise the IPA. Using the incipient boiling method, the mixture was gradually heated under low stirring speed with a hotplate with magnetic stirring until the first bubbles were observed. Once boiled, 0.1 N NaOH solution was added to the mix dropwise until the colour of the mixture changed from colourless to a faint pink.

2.6. FFA batch adsorption experiment

The FFA batch adsorption experiments were carried out in triplicate using a temperature-controlled water bath shaker (WiseBath® Shaking Water Bath, Witeg Labortechnik GmbH, Germany). For a typical experiment, 0.6 g of CS-0.5 was added into a 100 mL conical flask filled with 50 mL 50 mmol/L FFA solution. A total of 6 sets of conical flasks with the content mentioned above were prepared for each batch. The flasks were placed in the water bath shaker and shaken at 180 rpm at 45 °C. Each flask was removed from the water bath shaker every 10 min. The flask's content was then vacuum filtered, and 10 mL of the supernatant was immediately pipetted into another 100 mL conical flask with 10 ml of neutralised IPA for further analysis. The sample was titrated with 0.1 M NaOH using phenolphthalein as an indicator until the colour changed from colourless to pale pink for at least 30 s. The experiment was repeated using CS-1.0, CS-1.5, and HCl pre-treated RHA. The adsorption performances for each adsorbent were compared by referring to their respective adsorption capacity and FFA percentage removal, calculated using Equation (2): $Q_t = [(C_i - C_t) V] / W$ and (3): $\%FFA = (C_i - C_t) / c_i \times 100\%$ respectively, where Q_t (mmol/g) represents the adsorption capacity that denotes the amount of LA adsorbed per gram of adsorbent; %FFA (%) represents the percentage removal of LA; C_i and C_t (mmol/L) are the FFA concentrations at initial, i and time, t, respectively; V (L) as the volume of the FFA solution; and W (g) as the weight of adsorbent used.

2.7. Error analyses

To determine and validate the best-fitted model for kinetic and isotherm studies, statistical methods were applied to evaluate the fitness of the data, including the correlation coefficient (R^2), $R^2 = \frac{\sum (Q_{mean} - Q_{cal})^2}{\sum (Q_{cal} - Q_{mean})^2 + \sum (Q_{cal} - Q_{exp})^2}$; normalised standard deviation (ΔQ), $\Delta Q (\%) = \sqrt{\frac{\sum [(Q_{exp} - Q_{cal})/Q_{exp}]^2}{N - 1}} \times 100\%$ and chi-square test (χ^2), $\chi^2 = \sum_{i=1}^{n} \frac{(Q_{cal} - Q_{exp})^2}{Q_{cal}}$; Where Q_{exp} is the amount of adsorbate adsorbed during the adsorption experiment (mmol/g), Q_{cal} is the amount of adsorbate calculated from the kinetic or isotherm models (mmol/g), Q_{mean} is the mean value of the amount of adsorbate adsorbed (mmol/g), and N is the number of data points available.

3. Results and discussion

3.1. Material characterisations

The essential texture characteristics of both HCl pre-treated RHA and CS adsorbents, including the BET surface areas and BJH pore

information, are tabulated in Table 1. Meanwhile, Fig. 1 compares the N_2 adsorption-desorption isotherms and the hysteresis loops of the investigated samples. The notable distinct trends of the N_2 adsorption-desorption curves of all tested samples could be observed. HCl pre-treated RHA exhibited a combination of type I and IV isotherms with the H2 hysteresis loop [16]. Intriguingly, an earlier onset of N_2 adsorption for HCl pre-treated RHA indicated a predominantly microporous structure per IUPAC definitions. In contrast, all CS adsorbents (Fig. 1 (b – d)) exhibited significant changes in hysteresis loop shape and size, displaying type V isotherms with an H3 loop and an absence of a "knee" structure, as depicted in Fig. 1(a) [16]. The adsorption of nitrogen was also observed to increase gradually for CS adsorbents up to a higher relative pressure ($P/P_0 = 0.98$) as compared to HCl pre-treated RHA, with CS-1.0 displaying the largest hysteresis loop and highest nitrogen adsorption, as shown in Fig. 1(c). On top of that, the CS adsorbents showed loop closures at a relatively low relative pressure ($P/P_0 \sim 0.2–0.3$), giving rise to the sigmoid-type isotherms that suggested the occurrence of pore swelling during the analysis [17]. Such observation also indicated that all CS adsorbents could be associated with slit-shape pores [18], as evidenced by the morphologies in Fig. 3 (c – e).

On comparing the specific surface areas of CS adsorbents, CS-1.0 stood out with the most significant value at 216.47 m^2/g, surpassing CS-0.5 (19.69 m^2/g) and CS-1.5 (20.55 m^2/g). Such an observation could be attributed to structural alterations induced by the precipitation method [19]. Beyond the specific surface area, disparities existed in micropore and external surface areas between HCl pre-treated RHA and CS adsorbents. While HCl pre-treated RHA displayed a notable micropore surface area, CS adsorbents exhibited significant external surface areas. The formation of CS-1.0 involved the precipitation of extracted silicate with 1.0 M $Ca(OH)_2$, potentially blocking pores and aggregating on the surface [20]. The phenomenon generated extensive external structures with larger pore volumes, offering additional adsorption sites favourable for the LA molecules. At elevated $Ca(OH)_2$ concentration (1.5 M), the formation of impurities hampered the desired structure, leading to a reduced specific surface area, as observed in CS-1.5. The excessively introduced $Ca(OH)_2$ could potentially limit the adsorption due to the formation of a composite of calcium silicate and $Ca(OH)_2$, hence reducing the specific surface area of the resulting calcium silicate [21].

The FTIR spectra of HCl pre-treated RHA, CS-0.5, CS-1.0, and CS-1.5 are shown in Fig. 2. The characteristic adsorption peaks detected from 449 to 459 cm^{-1} indicate symmetric stretching and bending vibrations of Si–O groups, suggesting the presence of these groups in all synthesised samples [22]. The bands around 802–825 cm^{-1} corresponded to the stretching modes of O–Si–O bonds, attributing to the backbone silicate structure [23]. Interestingly, these bands were more intense in the HCl pre-treated RHA and decreased as $Ca(OH)_2$ concentrations in CS adsorbents increased. This shift is mainly attributed to the variation in the number of $(SiO)_3SiOH$, or "Q3" silicon, the silicon element connected with three bridging oxygen atoms, thus influencing non-bridging oxygen atoms and calcium ion interactions [24,25]. Such variation implies a cross-linking between neighbouring O–Si–O sheets among the CS adsorbents, suggesting the reconstruction of the silicate arrays due to the addition of calcium ions.

Interestingly, the Si–O–Ca functional groups were detected at 971, 962, and 953 cm^{-3}, exclusive to the CS adsorbents, mainly due to the addition of calcium during silicate extraction. Moreover, the peak at 972 cm^{-1} ascribed to the paired Si–OH group experienced a drastic decrease in intensity for all CS-adsorbents, further suggesting the progressive formation of the Si–O–Ca functional group [26]. These observations and the XRD results in Fig. 4(b) further supported the notion of a chain-silicate crystalline structure modified by Ca^{2+} [27]. The red shiftings of these bands were observed with increasing $Ca(OH)_2$ concentration, signifying a more significant interruption of the original amorphous silica-chain network by Ca^{2+}, leading to increased crystallinity and reduced surface area, as supported by the XRD and BET surface analyses results [28]. The bands at 3452, 3443, and 3422 cm^{-1} indicated the O–H bending vibration associated with hydroxyl groups and absorbed water. These functional groups confirm the presence of Si–O, H_2O, and O–H in synthesised adsorbents [29].

Fig. 3(a) depicts the morphology of the washed RH, showing well-arranged micro-bump structures. The non-porous structure was attributed to constituents in the RH, like lignin, hemicelluloses, and wax [30]. Fig. 3(b) shows that the transformation to a corn cob structure with loosely aggregated flake layers devoid of the micro-bump structures was linked to removing organic materials during acid pre-treatment, forming a porous structure [31]. Fig. 3(c), (d), and (e) illustrate the morphological changes of the CS adsorbents post-extraction. The CS adsorbents exhibited a crystalline structure characterised by regular geometric forms. At higher Ca^{2+} concentrations, CS adsorbents crumbled into smaller particles due to the formation of a gel-like structure induced by the presence of Ca^{2+} ions during the extraction process [32] before aggregating into reduced particle sizes due to the electrostatic interactions between silica and Ca^{2+} [33,34]. Differences in morphology were notable among CS samples, with CS-1.0 exhibiting greater porosity. This phenomenon could be attributed to reduced silicate chain length and interlayer spacing at increased $Ca(OH)_2$ concentration [24]. Additionally, a more significant proportion of foil-like sheet structures, layered side-to-side or edge-to-edge, on the surface of CS-1.0 suggested more open pores and adsorption sites, in line with its larger specific surface area [29].

The elemental composition analysis (Table 2) revealed insights into the composition changes of the synthesised materials. After the

Table 1
Surface analysis of HCl pre-treated RHA, CS-0.5, CS-1.0, and CS-1.5

Samples	S_{BET} (m^2/g)	S_{Micro} (m^2/g)	S_{Ex} (m^2/g)	V_T (cm^3/g)	V_{Micro} (cm^3/g)	DP (Å)
HCl Pre-treated RHA	238.64	177.84	60.79	0.1379	0.02489	54.17
CS-0.5	19.69	2.09	17.60	0.0910	0.10000	205.37
CS-1.0	216.47	21.97	194.50	0.6648	0.74000	105.83
CS-1.5	20.55	1.95	18.60	0.0939	0.11000	202.50

S_{BET}: BET specific surface area; S_{Micro}: t-plot micropore surface area; S_{Ex}: t-plot external surface area; V_T: Total pore volume; V_{micro}: Micropore volume; D_p: BJH desorption average pore diameter.
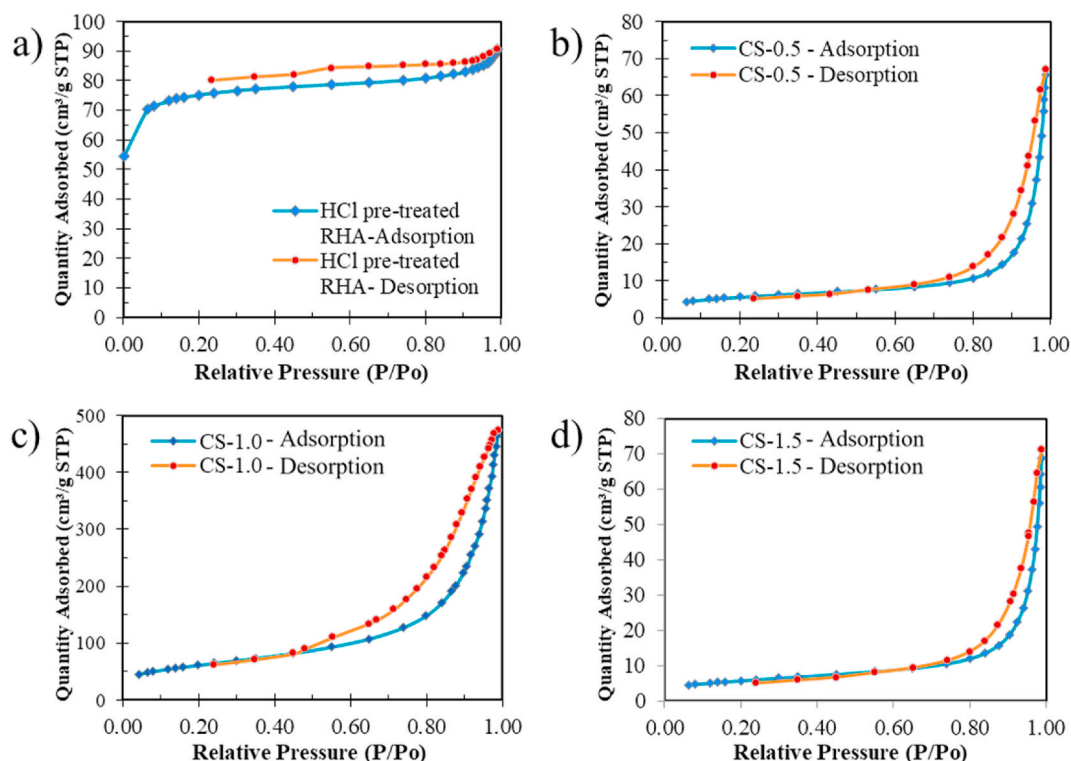
Fig. 1. N$_2$ adsorption-desorption isotherms of (a) HCl pre-treated RHA, (b) CS-0.5, (c) CS-1.0, and (d) CS-1.5.

HCl pre-treatment, oxygen content in RHA decreased significantly from 56.08% to 23.26%, indicating the successful removal of cellulose due to substantial acid leaching [35]. Surprisingly, the silica content decreased, and the carbon content increased after HCl pre-treatment of RHA. Such a phenomenon might be attributed to an inefficient combustion period during which higher combustion rates increased carbon content. On the other hand, the CS adsorbents contained predominantly oxygen, silicon, and calcium elements, as expected. Such lower silica content among the CS adsorbents compared to HCl pre-treated RHA could be elucidated as the influence of pH during the extraction process, leading to decreased silica activity and the elimination of bridging tetrahedra in the silicate chain [34]. Calcium content in CS adsorbents increased with higher concentrations of calcium precursor used, indicating an increased exchange of protons from the silanol group with calcium ions in the interlayer space of calcium silicate during extraction [36].

In Fig. 4, the XRD diffractogram showed a broad peak at $2\theta = 22°$, indicating the amorphous nature of the silica in HCl-pre-treated RHA [31]. The diffractograms in Fig. 4 also displayed well-defined sharp peaks, indicating the crystalline nature of CS adsorbents [37]. For all CS adsorbents, the characteristic peaks were identified with reference to International Centre for Diffraction Data (JCPDS) no. 00-044-1481 (Ca(OH)$_2$), JCPDS no. 00-014-0693 (CS), and JCPDS no. 00-019-0250 (CS hydrate). The characteristic peaks corresponding to Ca(OH)$_2$ were detected in all CS adsorbents, with higher concentrations of residual Ca(OH)$_2$ found in CS-1.5, suggesting the limiting binding site of the Ca^{2+} on the silicate chain due to its higher calcium concentration [23]. The excess Ca(OH)$_2$ residual that remained in CS-1.5 was more severe than that of CS-0.5 and CS-1.0. Semicrystalline structure peaks were observed, especially in CS-0.5 and CS-1.0, corresponding to porous foil-like sheet structures, while CS-1.5 exhibited fewer of these peaks [29]. Optimal synthesis conditions were therefore observed for CS-1.0, in which more semicrystalline structures and calcium silicate phases were detected, indicating better formation of porous foil-like sheet structures. In summary, XRD analysis confirmed the amorphous nature of silica in HCl pre-treated RHA and the successful production of crystalline CS adsorbents with varying degrees of semicrystalline structures.

The derivative mass loss profiles of RH, HCl pre-treated RHA and CS adsorbents from TGA are shown in Fig. 5. Significant differences in derivative weight loss can be identified among the tested materials. For ease of discussion, the essential derivative mass loss regions are marked as I (30–200 °C), II (200–400 °C), III (400–470 °C), and IV (630–780 °C). In Region I, mass losses were observed for all materials, corresponding to the release of light volatile compounds and capillary evaporation of water moisture in inner pores with thermal time lags [38,39]. The following region can be further separated into two zones, in which the first zone (200–300 °C) was attributed to the decomposition of cellulose and hemicellulose that is exclusive to RH only, while the second zone (300–400 °C) was resulted from the active and complete pyrolysis of hemicellulose from RH [39]. This region's missing derivative mass loss step for HCl-pretreated RHA and CS absorbents showed successful removal of cellulose, hemicellulose, and other impurities through acid pre-treatment. Next, the minor derivative mass loss in Region III was attributed to the complete pyrolysis of residual cellulose in RH [39]. Meanwhile, within Region III, all CS adsorbents experienced weight drops with increased intensity with corresponding calcium precursor concentrations (CS-0.5 < CS-1.0 < CS.-1.5). Such weight drop was associated with the dehydroxylation of the residual Ca
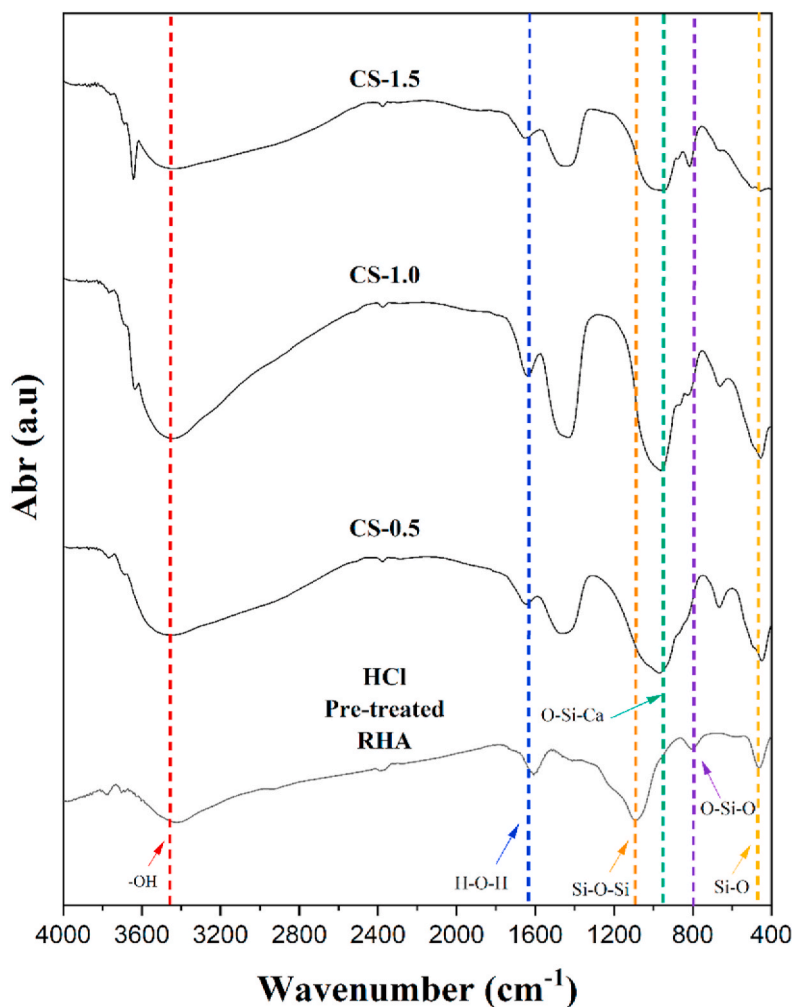
Fig. 2. FTIR spectra in HCl pre-treated RHA, CS-0.5, CS-1.0 and CS-1.5.

$(OH)_2$ for all CS absorbents [40]. A similar observation could also be identified in Region IV, where the weight drops increased with the corresponding calcium precursor concentrations. Attributed to the continuing dehydration of calcium silicates, such an observation is in line with the findings from FTIR and XRD analyses and further justifies the presence and successful precipitation of calcium silicates in all CS adsorbents [41].

3.2. Adsorption performances

The LA adsorption profiles were investigated as described in Section 2.6. As a baseline to the adsorption profiles, little to no LA adsorption throughout the experiment using HCl pre-treated RHA was intriguing. The adsorption capacities were recorded at zero for the first 50 min before increasing to 0.0831 ± 0.0004 mmol LA/g at the 60th minute. Despite its porous structure and high BET-specific surface area that suggest ample vacant adsorption sites, the low adsorption capacity might be attributed to the lack of suitable LA chemisorption sites on the HCl pre-treated RHA that was covered by mostly carbon elements, as shown by the EDS result. The carbon-covered silica on HCl pre-treated could not offer relevant adsorption sites to LA that was commonly adsorbed via hydrogen bonds, acid-base interaction or chemisorption [42].

The initial rapid LA adsorption phase (0–10 min) can be observed for all adsorbents except RHA, which shows little to no LA adsorption. Rapid adsorption was attributed to the abundance of vacant adsorption sites available at the initial stages, facilitating faster diffusion and adsorption [43,44]. After the first 10 min, the adsorption rates shown by all adsorbents dropped significantly until the Q_t values remained constant at the end of the experiment (1 h). The drop in rate was attributed to the reduction of the available vacant adsorption surface sites and the increased repulsive forces between the solute molecules on the adsorbent surface and the bulk phase [45]. Interestingly, the CS adsorbents reached equilibrium at other times: CS-0.5 at 60 min (2.4896 ± 0.0056 mmol LA/g), CS-1.0 at 40 min (2.5808 ± 0.0011 mmol LA/g), and CS-1.5 at 20 min (2.5833 ± 0.0036 mmol LA/g). The faster equilibrium time of CS-1.5 was attributed to neutralisation reactions between residual $Ca(OH)_2$ and LA, resulting in acid-base interaction, showing an
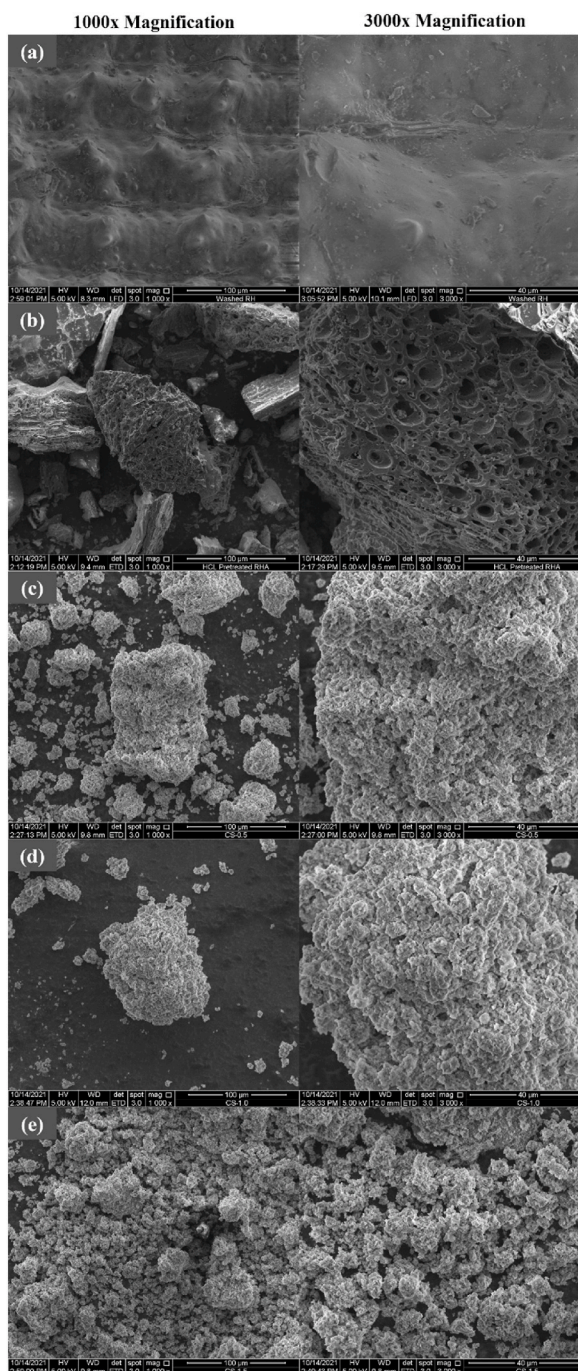
Fig. 3. SEM images of (a) washed RHA, (b) HCl pre-treated RHA, (c) CS-0.5, (d) CS-1.0, and (d) CS-1.5 at 1000x and 3000x magnification.

apparent LA adsorption instead [46]. On the other hand, the extended equilibrium periods taken by CS-0.5 and CS-1.0 might be attributed to the LA molecules' slow chemisorption onto the adsorbents [22].

Evidently, the BET analysis revealed that CS-1.0 had a significantly larger specific surface area (216.47 m^2/g) compared to CS-1.5 (20.55 m^2/g). A larger specific surface area allowed more adsorbates to be adsorbed, aligning with the higher LA removal efficiency in CS-1.0 [22]. Despite a smaller specific surface area, CS-1.5 showed 100% LA removal, suggesting that the significant amount of residual Ca(OH)$_2$ in CS-1.5 might have reacted with LA through acid-base neutralisation, thus enhancing its adsorption efficiency [47]. Furthermore, EDS analysis indicated that CS-1.5 had a higher calcium and oxygen component (15.09 and 69.53 atomic %, respectively) than CS-1.0 (10.52 and 61.51 atomic %, respectively), suggesting a significant amount of residual Ca(OH)$_2$ in CS-1.5. SEM analysis also showed that CS-1.0 had more foil-like sheet structures, potentially influencing better adsorption performance, as opposed
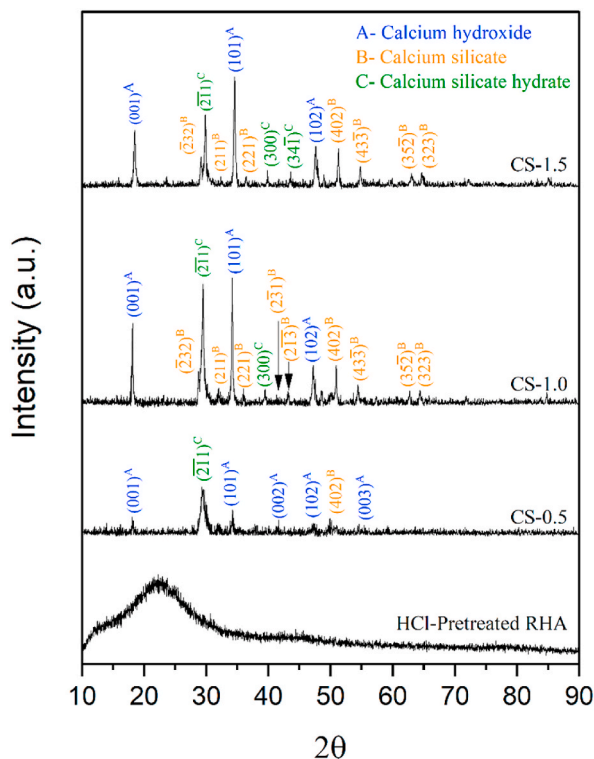
Fig. 4. XRD diffractograms of HCl pre-treated RHA and CS adsorbents.

Table 2
Element composition of washed RH, HCl pre-treated RHA, CS-0.5, CS-1.0 and CS-1.5

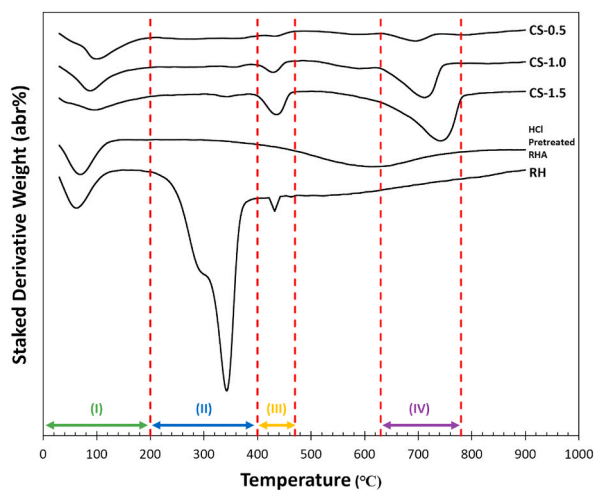| Samples	Element (Atomic %)				
	C	O	Si	Na	Ca
Washed RH	32.95	56.08	10.79	–	–
HCl pre-treated RHA	71.59	23.26	5.15	–	–
CS-0.5	–	71.22	4.01	4.01	11.50
CS-1.0	21.28	61.51	5.72	0.59	10.52
CS-1.5	7.97	69.53	4.65	3.76	15.09

Fig. 5. TG profiles for RH, HCl pre-treated RHA and CS adsorbents.

to that of CS-1.5. As the neutralisation reactions in CS-1.5 rendered the recovery of LA through neutralisation useless, CS-1.0 was selected as the best-performing adsorbent due to its large specific surface area and insignificant Ca(OH)$_2$ residual. Hence, it was used for further investigation in this study.

3.3. Significant parameter study

Fig. 6 shows the effect of adsorbent dosage on the LA removal efficiency and adsorption capacity using CS-1.0 with 30 mmol/L LA solution at 45 °C for 10 min. Generally, the LA removal percentage showed an increasing trend at higher adsorbent dosages, i.e. from 0.2 g to 1.0 g. The highest removal efficiency (100%) was achieved by 0.8 g and 1.0 g of adsorbent dosage, while the lowest LA removal (74.19%) occurred when 0.2 g adsorbent dosage was used. However, the highest adsorption capacity (5.6712 ± 0.0016 mmol LA/g) was obtained at 0.2 g adsorbent dosage, while the lowest adsorption capacity (1.5532 ± 0.0023 mmol LA/g) was achieved with a 1.0 g adsorbent dosage. Generally, the increased available adsorption sites with higher adsorbent dosage led to more significant LA adsorption [48]. Such a trend was aligned with the known behaviours of adsorbents, where a finite number of active sites led to eventual saturation and the limit on maximum removal capacity [49,50].

The effect of initial LA concentration on LA removal efficiency and adsorption capacity using 0.6 g CS-1.0 at 45 °C for 10 min is illustrated in Fig. 7. Changing the initial concentration from 10 to 50 mmol/L led to a gradual decrease in removal efficiency from 100% (10 mmol/L) to 90% (50 mmol/L). On the contrary, the highest adsorption capacity (3.7112 ± 0.0014 mmol LA/g) was achieved at 50 mmol concentration, while the lowest adsorption capacity (0.8302 ± 0.0026 mmol LA/g) was achieved at 10 mmol concentration. Such a trend could be attributed to the less competitive adsorption, as the limited LA interacts with widely available adsorption sites at low concentrations. However, at higher initial acid concentrations, a lower ratio of initial acid molecules to accessible adsorption sites occurred. Hence, the unadsorbed residual LA molecules remained in the solution, resulting in a lower removal percentage [51]. On the other hand, the increase in LA adsorption capacity with higher initial concentration could be attributed to the enhancement in the driving force of the concentration gradient [52–54].

Fig. 8 demonstrates the effect of adsorption temperature on LA removal efficiency and adsorption capacity using 0.6 g CS-1.0 and 30 mmol/L LA solution for 10 min. Interestingly, both LA removal efficiency and adsorption capacity increased as adsorption temperature increased. The highest removal efficiency (100%) and adsorption capacity (2.5756 ± 0.0015 mmol LA/g) were achieved at 50 and 60 °C, while the lowest (90.32% and 2.3225 ± 0.0101 mmol LA/g) at 30 °C. Such a trend could be elucidated as the endothermic adsorption nature that contributed to higher removal efficiency at higher temperatures [55]. Higher temperatures were therefore favoured to overcome the stronger intermolecular forces between LA molecules and the CS-1.0 surface compared to the interaction between LA molecules and solvent [56]. A similar trend was observed in the fluoride adsorption study on activated coconut shell carbon, montmorillonite clay, and rice husk ash [57]. It was reported that the higher removal efficiency at higher temperatures could be attributed to the increased kinetic energy of adsorbate molecules and improved mobility onto adsorbents.

3.4. Adsorption kinetics

The studies of adsorption kinetics models are essential to establish the contact time necessary to achieve equilibrium and are critical
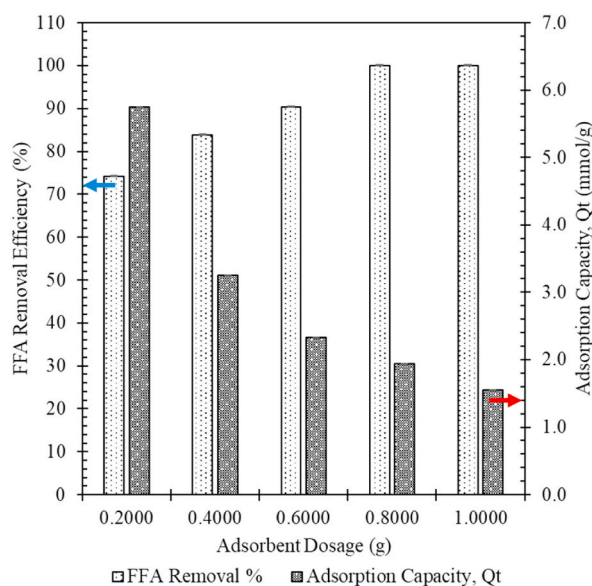

Fig. 6. Lauric acid removal efficiencies and adsorption capacities after 10 min using different CS-1.0 adsorbent dosages at 30 mmol/L initial LA concentrations and 45 °C.
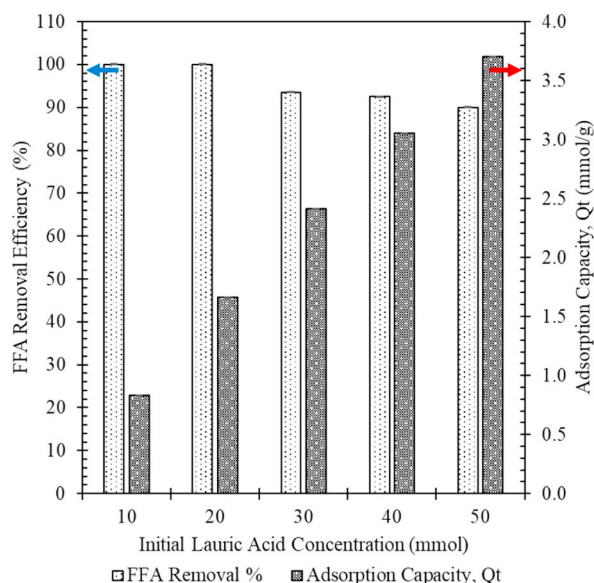
Fig. 7. Lauric acid removal efficiencies and adsorption capacities after 10 min using various initial LA concentrations and 0.6g CS-1.0 at 45 °C.
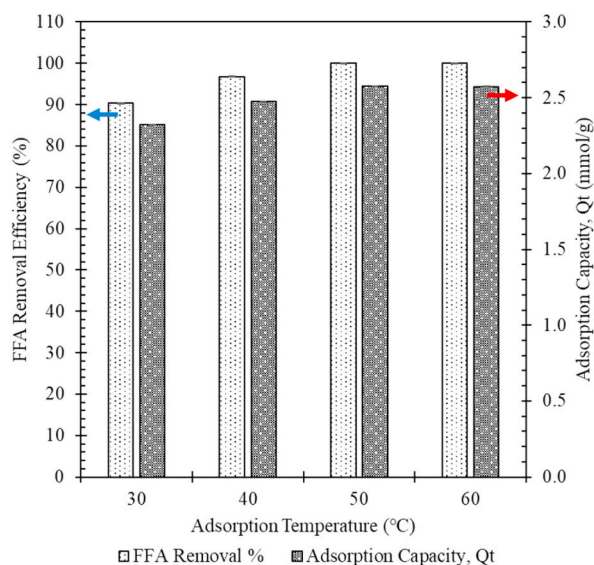

Fig. 8. Lauric acid removal efficiencies and adsorption capacities after 10 min using various adsorption temperatures at 30 mmol/L LA concentrations and 0.6g CS-1.0.

in revealing the adsorption process's kinetics and determining the linkage between the material structure and the adsorption performance [58]. The selected adsorption kinetics models for investigation in this study, including pseudo-first-order (PFO), pseudo-second-order (PSO), Elovich (EVE), and intraparticle diffusion model (IPD), were linearised, and the equations, kinetic parameters, and error analyses result for LA adsorption onto CS-1.0 are summarised in Table 3.

All linearised kinetic models were fitted with experiment data and are plotted in Fig. 9 (a – d), together with the respective parity plots in Fig. 9 (i – iv) to illustrate the agreement between the experiment and calculated data. Based on the results observed from linearised kinetic model fitting, parity plots, and error analyses, a comprehensive understanding of the adsorption kinetic of LA onto CS-1.0 could be discussed. Generally, the PSO model had the highest R^2 value (0.9959), followed by PFO (0.9716), IPD (0.9683), and EVE (0.9068), indicating good fits for all models ($R^2 > 0.90$) [59,60]. Despite PSO having the highest R^2 value, the ΔQ % and χ^2 values for the IPD model were significantly lower, suggesting a better agreement between the calculated and experimental values than the rest of the models. IPD had the lowest ΔQ value (2.2183%) and χ^2 value (0.0043), indicating its suitability in describing the adsorption process. The parity plot further supported the claim, illustrating the agreement between experimental and calculated Q_t values for each

Table 3
Linearised kinetic parameters and error analyses for lauric acid adsorption onto CS-1.0

Model	Equation	Parameters	Values
Pseudo-first-order (PFO)	$ln(Q_e - Q_t) = ln\,Q_e - k_1 t$	k_1 (min^{-1})	0.0731
		$Q_{e,cal}$ (mmol g^{-1})	0.6791
		$Q_{e,\,exp}$ (mmol g^{-1})	1.7061
		R^2	0.9716
		ΔQ (%)	83.7758
		χ^2	32.8700
Pseudo-second-order (PSO)	$\frac{t}{Q_t} = \frac{1}{k_2 Q_e^2} + \frac{1}{Q_e}\,t$	k_2 (g mmol^{-1} min^{-1})	0.2981
		$Q_{e,cal}$ (mmol g^{-1})	0.6791
		$Q_{e,\,exp}$ (mmol g^{-1})	1.7061
		R^2	0.9959
		ΔQ (%)	11.4406
		χ^2	0.1190
Elovich (EVE)	$Q_t = \frac{1}{b} ln(ab) + \frac{1}{b} ln\,t$	a (mmol g^{-1} min^{-1})	33.0980
		b (g mmol^{-1})	5.3824
		R^2	0.9068
		ΔQ (%)	4.2158
		χ^2	0.0140
Intraparticle diffusion (IPD)	$Q_t = k_{id} t^{\frac{1}{2}} + C_i$	k_{id} (mmol g^{-1} min$^{0.5}$)	0.1250
		C_i (mmol g^{-1})	0.9625
		R^2	0.9683
		ΔQ (%)	2.2183
		χ^2	0.0043

model.

The best-fitted IPD model suggested the significant role of the LA molecules' diffusion into the pores of CS-1.0 in the rate-determining step [45]. This conclusion aligned with the idea that less-fitted models like PFO, PSO, and EVE primarily consider chemical interactions and surface adsorption without accounting for diffusion [61]. Hence, a three-step diffusive LA adsorption onto CS-1.0 was proposed: (a) diffusion of LA molecules through the liquid film surrounding the particles, (b) internal diffusion into large and small pores, and (c) adsorption onto active sites within the pores of calcium silicate particles. Indeed, the slowest step, i.e. internal diffusion, determined the adsorption rate [62]. More evidence could be identified from Fig. 8(d), in which only the linear part of the steep-sloped, linear, and plateau portions of Weber–Morris plots could be observed [63].

Where Q_e and Q_t (mmol/g) represent the corresponding adsorption capacity for lauric acid adsorbed onto CS-1.0 at equilibrium, e and time, t; t represents the time taken for the adsorption process (min); k_1 represents the adsorption constant for PFO model; k_2 represents the adsorption constant for PSO model; a is the y-intercept of the straight line, while b is the slope of the graph for EVE plot; k_{id} represents the IPD rate constant (mmol/g min$^{1/2}$), while C_i represents the constant corresponding to the boundary layer thickness, which is determined from the y-intercept of the straight line (mmol/g).

3.5. Adsorption isotherms

Investigating the adsorption isotherms is critical for establishing an equation that appropriately represents the data and could be utilised for design purposes. The data fitting results for the linearised Langmuir, Freundlich, Temkin, and Dubinin–Radushkevich isotherms are summarised in Table 4, while the curve fit and parity plots are plotted in Fig. 10 (a – d) and Fig. 10 (i – iv), respectively. A comprehensive evaluation of the fitted isotherms was done based on the error analyses reported in this study. Despite variations in R^2 values were observed, all four models displayed high R^2 values ($R^2 > 0.90$), which signified a strong fit between the models and the experimental data [59,64]. Meanwhile, the statistical error analysis shows that the trends in both ΔQ and χ^2 values mirrored the R^2 values. The Freundlich isotherm had the lowest ΔQ (8.2813%) and χ^2 (0.0573) values, indicating better fit and consistency with experimental data, collectively pointing toward the Freundlich isotherm as the better-fitting model. Such findings were consistent with previous studies where similar observations were reported [22,65].

The excellent fit of the Freundlich isotherm suggested that the adsorption sites on the CS-1.0 surface were truly heterogeneous, in which multiple layers of adsorbed LA species could form on the surface through unidentate and bidentate coordination, implying the potential for infinite adsorption during the process [66]. Hence, the proposed adsorption mechanism should involve the complexation and hydrogen bonding between the carboxylate ions of LA and the calcium ions of CS-1.0 [67]. Additionally, the formation of hydrogen bonds between the carbonyl oxygen of LA and the silanol groups on CS-1.0's surface further contributed to the said adsorption [68]. The low mean adsorption energy (E = 4.7204 kJ mol^{-1}, below 8 kJ mol^{-1}) calculated using Dubinin–Radushkevich isotherm further supports the physical interaction of the adsorption, in which the adsorbent and adsorbate were proposed to be hydrogen-bonded [69]. Meanwhile, the heterogeneous nature of the CS-1.0 surface, leading to varying affinities of different surface locations for LA molecules, could also be deduced [59]. Such a phenomenon could result in uneven adsorption modes, including monolayer, multilayer, and even zero adsorption. Therefore, the poor fit of the Langmuir isotherm data was probably due to the highly heterogeneous surface of the calcium silicate structure [70]. Similar findings were also reported, in which weak interactions between FFA and montmorillonite were reported, and the adsorption process follows the Freundlich isotherm rather than the Langmuir
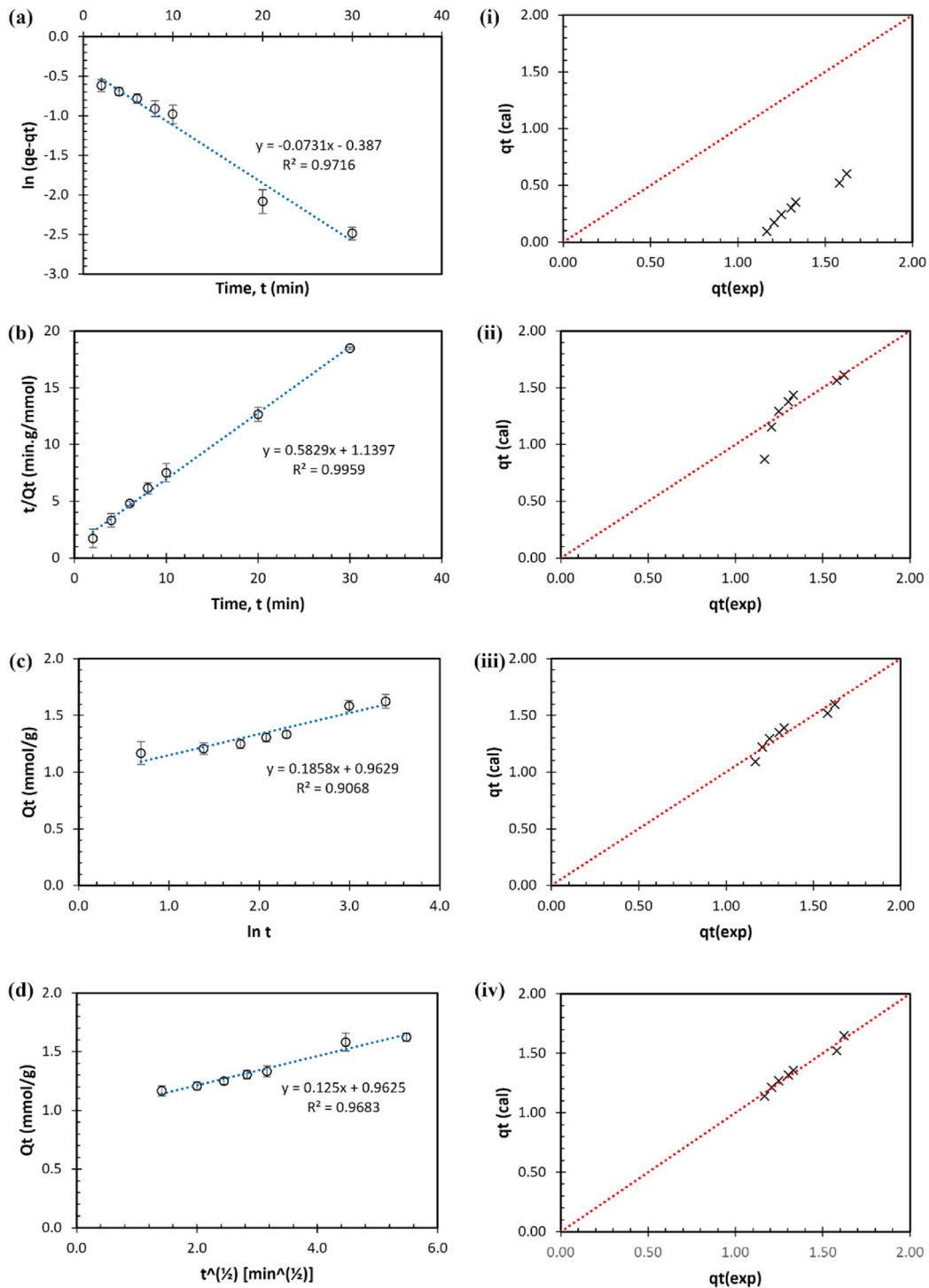
Fig. 9. Linearised and parity plots of (a, i) PFO, (b, ii) PSO, (c, iii) EVE and (d, iv) IPD kinetic models for the lauric acid adsorption onto CS-1.0.

isotherm, indicating that multilayer adsorption occurred on the heterogeneous adsorbent surface [71].

Where C_e is the equilibrium concentration of lauric acid in the solution (mmol/L); Q_e is the adsorption capacity for the equilibrium amount of lauric acid uptake onto the CS-1.0 (mmol/g); Q_m is the maximum adsorption capacity (mmol/g), b is the Langmuir constant related to the affinity of binding sites (L/mmol); n and K_F are the Freundlich constants related to the corresponding adsorption intensity and adsorption capacity, respectively; B_T represents the adsorption heat constant for Temkin isotherm; K_T represents the Temkin adsorption potential (L/g); β represents the activity coefficient related to the mean free energy of adsorption; E represents the

Table 4

Linearised adsorption isotherm parameters and error analyses for lauric acid adsorption onto CS-1.0

Model	Equation	Parameters	Values
Langmuir	$\dfrac{C_e}{Q_e} = \dfrac{1}{Q_m b} + \dfrac{1}{Q_m}\,C_e$	b (L mmol^{-1})	0.0527
		Q$_m$ (mmol g^{-1})	2.1568
		Q$_{e,cal}$ (mmol g^{-1})	3.4990
		Q$_{e,\,exp}$ (mmol g^{-1})	3.1836
		R^2	0.9337
		ΔQ (%)	9.3006
		χ^2	0.0996
Freundlich	$log\,Q_e = log\,K_F + \dfrac{1}{n}\,log\,C_e$	n	0.6207
		K$_F$ (mmol$^{(1-1/n)}$ L$^{(1/n)}$ g^{-1})	0.0598
		Q$_{e,cal}$ (mmol g^{-1})	3.1696
		Q$_{e,\,exp}$ (mmol g^{-1})	3.1836
		R^2	0.9871
		ΔQ (%)	8.2813
		χ^2	0.0573
Temkin	$Q_e = B_T\,ln\,K_T + B_T\,ln\,C_e$	B$_T$	2.2634
		K$_T$ (L mmol^{-1})	0.3030
		Q$_{e,cal}$ (mmol g^{-1})	2.8745
		Q$_{e,\,exp}$ (mmol g^{-1})	3.1836
		R^2	0.9646
		ΔQ (%)	29.9585
		χ^2	0.3666
Dubinin–Radushkevich	$ln\,Q_e = ln\,Q_m - \beta\varepsilon^2$	Q$_m$ (mmol g^{-1})	47.4654
		β (× 10^{-8} mol^2 kJ^{-2})	2.2439
		E (kJ mol^{-1})	4.7204
		R^2	0.9122
		ΔQ (%)	21.1599
		χ^2	0.3451

mean adsorption energy.

3.6. Adsorption thermodynamics

The study of adsorption thermodynamics allows further understanding of the adsorption of LA onto CS-1.0 as a macroscopic phenomenon. It enables the prediction of the said adsorption once the crucial thermodynamic properties such as Gibbs free energy change (ΔG°), enthalpy (ΔH°), and entropy (ΔS°) are obtained [72]. For that purpose, the thermodynamic plot for LA adsorption onto CS-1.0 is presented in Fig. 11. The values of ΔG°, ΔH°, and ΔS° can be calculated by applying Van's Hoff equation ($\Delta G° = -RT\,ln\,K_d$) and Gibbs-Helmholtz relationship ($\Delta G° = \Delta H° - T\Delta S°$), where $K_d = (c_0 - c_e)/c_e$ and represents a temperature-sensitive distribution constant dependence on the difference of stoichiometric coefficients; c_0 represents initial LA concentration (mmol/L); c_e represents LA concentration at equilibrium (mmol/L); R represents ideal gas constant (8.3142 J K^{-1} mol^{-1}); and T represents absolute temperature (K). The negative gradient of the thermodynamic plot indicated the endothermic nature of LA adsorption onto CS-1.0 with ΔH° = 85.525 kJ mol^{-1} K^{-1}. At low adsorption temperature, the positive value of ΔS° (0.2948 kJ mol^{-1}) and negative values of ΔG° (−3.8306, −6.7782, −9.7258, −12.6733 kJ mol^{-1} K^{-1} at 30, 40, 50, 60 °C, respectively) indicated the spontaneous nature of the adsorption in this study.

3.7. Potential industrial application for waste frying oil remediation

The graphical abstract illustrates the proposed FFA extraction from WFO using RHA-based calcium silicates (CS-1.0), up-scaled to be part of the industrial-level waste management system. Principally, in Stage 1, an adsorption tower packed with an appropriate amount of CS-1.0 would be fed with the stream of filtered WFO containing unwanted FFAs to remove them from the stream via adsorption at an optimum ratio, stream feed rate, and temperature. Upon reaching equilibrium, CS-1.0 should then be saturated with the adsorbed FFAs, and the operation would move to Stage 2, in which the CS-1.0 was removed via desorption, at the same time, recovering the adsorbed FFA for sales before CS-1.0 was reused again in a loop.

4. Conclusions

The novel alkaline earth metal silicates were successfully synthesised from RH, an agricultural waste readily available in abundance for effective lauric acid adsorption, one of the common constituents in the ecotoxic WFO. Surface and phase analyses showed the successful synthesis of CS adsorbents, especially for CS-0.10, which had a high specific surface area (216.47 m^2/g) and lack of excess Ca (OH)$_2$ residual that could hamper the desired structure and led to undesired pore blockage. Unlike HCl pre-treated RHA, CS-1.0 contained high silicate purity, high porosity, large pore volume, and foil-like sheet structure with increased adsorption sites eluci- dated to be advantageous for LA adsorption. LA adsorption equilibrium was achieved at 40 min with 2.5808 ± 0.0011 mmol LA/g
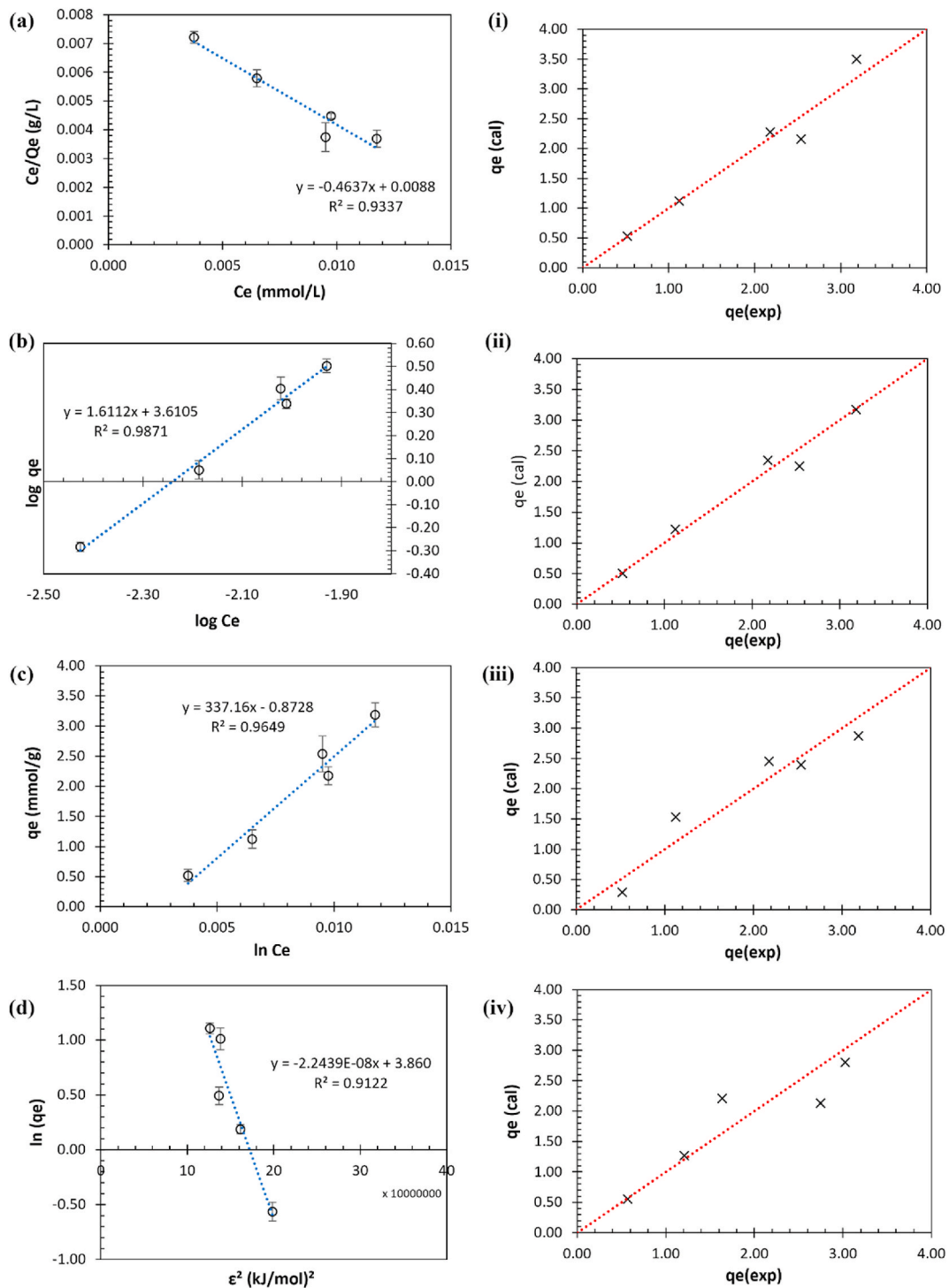
Fig. 10. Linearised and parity plots of (a, i) Langmuir, (b, ii) Freudlich, (c, iii) Temkin, and (d, iv) Dubinin–Radushkevich isotherms for the lauric acid adsorption onto CS-1.0.

adsorption capacity for CS-1.0, making it the best performing among all adsorbents tested, including the HCl pre-treated RHA. Significant improvement in terms of adsorption capacity was observed when compared to that of HCl pre-treated RHA. A gradual increase in LA removal and decreased adsorption capacities at higher initial LA concentrations were observed, attributed to the greater driving force for adsorption. An opposite trend was observed when the dosage was altered, elucidated by the availability of the accessible adsorption sites on CS-1.0. The intraparticle diffusion (IPD) model satisfactorily describes the adsorption in the study, with k_{id} of
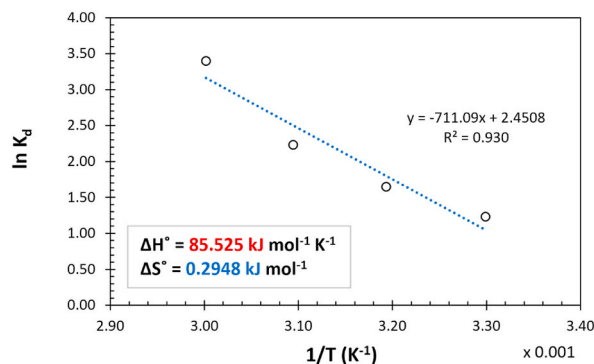
Fig. 11. Thermodynamic plot of $\ln K_d$ vs. $1/T$ for lauric acid adsorption onto CS-1.0.

$0.1250 \, \text{mmol g}^{-1} \, \text{min}^{0.5}$ and C_i of $0.9625 \, \text{mmol g}^{-1}$. Freudlich isotherm was also evaluated to fit the experimental adsorption data with high R^2 (0.9871) and low ΔQ (8.2813%) and χ^2 (0.0753) values, showing comparatively high $Q_{e,cal}$ value ($3.1696 \, \text{mmol g}^{-1}$). The thermodynamic study also indicates the spontaneous and endothermic LA adsorption onto CS-1.0 with $\Delta H° = 85.525 \, \text{kJ mol}^{-1} \, \text{K}^{-1}$, $\Delta S° = 0.2948 \, \text{kJ mol}^{-1}$, and negative $\Delta G°$ values. A potential industrial application of the developed CS-1.0 for WFO remediation was also proposed.

Data availability statement

The authors verified that the data associated with this study has not been deposited into any publicly available repository. The data supporting this study's findings are available from the corresponding author, Pengyong Hoo, upon reasonable request.

CRediT authorship contribution statement

Zainor Syahira Zainal: Writing – original draft, Validation, Methodology, Investigation, Formal analysis. **Pengyong Hoo:** Writing – original draft, Visualization, Supervision, Resources, Project administration, Investigation, Funding acquisition, Conceptualization. **Abdul Latif Ahmad:** Writing – review & editing, Supervision, Resources, Project administration, Funding acquisition, Conceptualization. **Ahmad Zuhairi Abdullah:** Writing – review & editing, Supervision, Resources, Project administration, Funding acquisition, Conceptualization. **Qihwa Ng:** Writing – review & editing, Visualization, Funding acquisition, Formal analysis. **Siewhoong Shuit:** Writing – review & editing, Resources, Funding acquisition, Formal analysis. **Siti Kartini Enche Ab Rahim:** Writing – review & editing, Funding acquisition, Formal analysis. **Jeyashelly Andas:** Writing – review & editing, Funding acquisition, Formal analysis.

Declaration of competing interest

The authors declare the following financial interests/personal relationships which may be considered as potential competing interests: Pengyong Hoo reports financial support was provided by Malaysia Ministry of Higher Education.

Acknowledgements

References

[1] S.S. Shukla, R. Chava, S. Appari, A. Bahurudeen, B.V.R. Kuncharam, Sustainable use of rice husk for the cleaner production of value-added products, J. Environ. Chem. Eng. 10 (1) (2022) 106899, https://doi.org/10.1016/j.jece.2021.106899.

[2] Y. Shen, Rice husk silica derived nanomaterials for sustainable applications, Renew. Sustain. Energy Rev. 80 (2017) 453–466, https://doi.org/10.1016/j.rser.2017.05.115.

[3] X. Liu, X. Chen, L. Yang, H. Chen, Y. Tian, Z. Wang, A review on recent advances in the comprehensive application of rice husk ash, Res. Chem. Intermed. 42 (2016) 893–913, https://doi.org/10.1007/s11164-015-2061-y.

[4] R. Pode, Potential applications of rice husk ash waste from rice husk biomass power plant, Renew. Sustain. Energy Rev. 53 (2016) 1468–1485, https://doi.org/10.1016/j.rser.2015.09.051.

[5] T.-H. Liou, Y.H. Liou, Utilization of rice husk ash in the preparation of graphene-oxide-based mesoporous nanocomposites with excellent adsorption performance, Materials 14 (5) (2021) 1214, https://doi.org/10.3390/ma14051214.

[6] S.S. Hossain, P. Roy, C.-J. Bae, Utilization of waste rice husk ash for sustainable geopolymer: a review, Construct. Build. Mater. 310 (2021) 125218, https://doi.org/10.1016/j.conbuildmat.2021.125218.

[7] L.T. Schneider, G. Bonassa, H.J. Alves, T.R.W. Meier, E.P. Frigo, J.G. Teleken, Use of rice husk in waste cooking oil pre-treatment, Environ. Technol. 40 (5) (2019) 594–604, https://doi.org/10.1080/09593330.2017.1397772.

[8] Y. Zou, T. Yang, Rice husk, rice husk ash and their applications, in: Rice Bran and Rice Bran Oil, Elsevier, 2019, pp. 207–246.

[9] R.A. Bakar, R. Yahya, S.N. Gan, Production of high purity amorphous silica from rice husk, Procedia Chem. 19 (2016) 189–195, https://doi.org/10.1016/j.proche.2016.03.092.

[10] P. Chen, W. Gu, W. Fang, X. Ji, R. Bie, Removal of metal impurities in rice husk and characterization of rice husk ash under simplified acid pre-treatment process, Environ. Prog. Sustain. Energy 36 (3) (2017) 830–837, https://doi.org/10.1002/ep.12513.

[11] A. Farook, S. Ravendran, Saturated fatty acid adsorption by acidified rice hull ash, J. Am. Oil Chem. Soc. 77 (2000) 437–440, https://doi.org/10.1007/s11746-000-0070-0.

[12] M.C. Manique, C.S. Faccini, B. Onorevoli, E.V. Benvenutti, E.B. Caramão, Rice husk ash as an adsorbent for purifying biodiesel from waste frying oil, Fuel 92 (1) (2012) 56–61, https://doi.org/10.1016/j.fuel.2011.07.024.

[13] W. Clowutimon, P. Kitchaiya, P. Assawasaengrat, Adsorption of free fatty acid from crude palm oil on magnesium silicate derived from rice husk, Eng. J. 15 (3) (2011) 15–26, https://doi.org/10.4186/ej.2011.15.3.15.

[14] P. Assawasaengrat, P. Jintanavasan, P. Kitchaiya, Adsorption of FFA, soap and glycerine in biodiesel using magnesium silicate, Chem. Eng. Trans. 43 (2015) 1135–1140, https://doi.org/10.3303/CET1543190.

[15] R. Phuttawong, N. Chantaramee, P. Pookmanee, K. Puntharod, Synthesis and characterization of calcium silicate from rice husk ash and shell of snail Pomacea Canaliculata by solid state reaction, Adv. Mater. Res. 1103 (2015) 1–7, https://doi.org/10.4028/www.scientific.net/AMR.1103.1.

[16] M. Thommes, K. Kaneko, A.V. Neimark, J.P. Olivier, F. Rodriguez-Reinoso, J. Rouquerol, K.S. Sing, Physisorption of gases, with special reference to the evaluation of surface area and pore size distribution (IUPAC Technical Report), Pure Appl. Chem. 87 (9–10) (2015) 1051–1069, https://doi.org/10.1515/pac-2014-1117.

[17] P. Maziarka, C. Wurzer, P.J. Arauzo, A. Dieguez-Alonso, O. Mašek, F. Ronsse, Do you BET on routine? The reliability of N_2 physisorption for the quantitative assessment of biochar's surface area, Chem. Eng. J. 418 (2021) 129234, https://doi.org/10.1016/j.cej.2021.129234.

[18] F. Adam, P. Retnam, A. Iqbal, The complete conversion of cyclohexane into cyclohexanol and cyclohexanone by a simple silica-chromium heterogeneous catalyst, Appl. Catal. A-Gen. 357 (1) (2009) 93–99, https://doi.org/10.1016/j.apcata.2009.01.017.

[19] P. Terzioğlu, S. Yücel, Synthesis of magnesium silicate from wheat husk ash: effects of parameters on structural and surface properties, Bioresources 7 (2012) 5435–5447, https://doi.org/10.15376/biores.7.4.5435-5447.

[20] H. Beglaryan, N. Zulumyan, A. Isahakyan, S. Melikyan, A. Terzyan, Study of the interaction between calcium hydroxide and amorphous silica obtained from serpentinites, Russ. J. Phys. Chem. A 93 (2019) 924–931, https://doi.org/10.1134/S0036024419050042.

[21] E. Fratini, M.G. Page, R. Giorgi, H. Cölfen, P. Baglioni, B. Demé, T. Zemb, Competitive surface adsorption of solvent molecules and compactness of agglomeration in calcium hydroxide nanoparticles, Langmuir 23 (5) (2007) 2330–2338, https://doi.org/10.1021/la062023i.

[22] M. Wang, B. Wen, B. Fan, H. Zhang, Study on adsorption mechanism of silicate adsorbents with different morphologies and pore structures towards formaldehyde in water, Colloids Surf. A Physicochem. Eng. Asp. 599 (2020) 124887, https://doi.org/10.1016/j.colsurfa.2020.124887.

[23] A. Meiszterics, L. Rosta, H. Peterlik, J. Rohonczy, S. Kubuki, P. Henits, K. Sinkó, Structural characterization of gel-derived calcium silicate systems, J. Phys. Chem. A 114 (38) (2010) 10403–10411, https://doi.org/10.1021/jp1053502.

[24] J. Li, Q. Yu, H. Huang, S. Yin, Effects of Ca/Si ratio, aluminum and magnesium on the carbonation behavior of calcium silicate hydrate, Materials 12 (8) (2019) 1268, https://doi.org/10.3390/ma12081268.

[25] Y. Zhou, H. Zheng, Y. Qiu, X. Zou, J. Huang, A Molecular Dynamics Study on the Structure, Interfaces, Mechanical Properties, and Mechanisms of a Calcium Silicate Hydrate/2D-Silica Nanocomposite, vol. 7, 2020, https://doi.org/10.3389/fmats.2020.00127.

[26] L. Peng, W. Qisui, L. Xi, Z. Chaocan, Investigation of the states of water and OH groups on the surface of silica 334 (1) (2009) 112–115, https://doi.org/10.1016/j.colsurfa.2008.10.028.

[27] R. Ellerbrock, M. Stein, J. Schaller, Comparing amorphous silica, short-range-ordered silicates and silicic acid species by FTIR, Sci. Rep. 12 (1) (2022) 11708, https://doi.org/10.1038/s41598-022-15882-4.

[28] E. John, D. Stephan, Calcium silicate hydrate—in-situ development of the silicate structure followed by infrared spectroscopy, J. Am. Ceram. Soc. 104 (12) (2021) 6611–6624, https://doi.org/10.1111/jace.18019.

[29] X. Wang, J. Sun, Y. Zhang, Y. Zhang, Study on the correlation between pore morphology of porous calcium silicate and high-capacity formaldehyde adsorption, Environ. Technol. 42 (13) (2021) 2021–2030, https://doi.org/10.1080/09593330.2019.1687588.

[30] N.R. Rajendran Royan, A.B. Sulong, N.Y. Yuhana, R.S. Chen, M.H. Ab Ghani, S. Ahmad, UV/O3 treatment as a surface modification of rice husk towards preparation of novel biocomposites, PLoS One 13 (5) (2018) e0197345, https://doi.org/10.1371/journal.pone.0197345.

[31] P. Deshmukh, J. Bhatt, D. Peshwe, S. Pathak, Determination of silica activity index and XRD, SEM and EDS studies of amorphous SiO_2 extracted from rice husk ash, Trans. Indian Inst. Met. 65 (2012) 63–70, https://doi.org/10.1007/s12666-011-0071-z.

[32] S. Liu, S. Cui, H. Guo, Y. Wang, Y. Zheng, Adsorption of lead ion from wastewater using non-crystal hydrated calcium silicate gel, Materials 14 (4) (2021) 842–853, https://doi.org/10.3390/ma14040842.

[33] S.J. Liu, S.P. Cui, H.X. Guo, Y.L. Wang, N. Li, Y.L. Gan, Y. Zheng, Preparation of hydrated calcium silicate gel and its adsorption properties for Cu (II), Mater. Sci. Forum 993 (2020) 1445–1449, https://doi.org/10.4028/www.scientific.net/MSF.993.1445.

[34] K. Zheng, N. Taccardi, A.M. Beltrán, B. Sui, T. Zhou, V.R. Marthala, M. Hartmann, A.R. Boccaccini, Timing of calcium nitrate addition affects morphology, dispersity and composition of bioactive glass nanoparticles, RSC Adv. 6 (97) (2016) 95101–95111, https://doi.org/10.1039/C6RA05548F.

[35] S. Azat, Z. Sartova, K. Bekseitova, K. Askaruly, Extraction of high-purity silica from rice husk via hydrochloric acid leaching treatment, Turk. J. Chem. 43 (5) (2019) 1258–1269, https://doi.org/10.3906/kim-1903-53.

[36] B. Lothenbach, A. Nonat, Calcium silicate hydrates: solid and liquid phase composition, Cement Concr. Res. 78 (2015) 57–70, https://doi.org/10.1016/j.cemconres.2015.03.019.

[37] M. Mansha, S.H. Javed, M. Kazmi, N. Feroze, Study of rice husk ash as potential source of acid resistance calcium silicate, Adv. Chem. Eng. Sci. 1 (3) (2011) 147–153, https://doi.org/10.4236/aces.2011.13022.

[38] K. Garbev, M. Bornefeld, G. Beuchle, P. Stemmermann, Cell dimensions and composition of nanocrystalline calcium silicate hydrate solid solutions. Part 2: X-ray and thermogravimetry study, J. Am. Ceram. Soc. 91 (9) (2008) 3015–3023, https://doi.org/10.1111/j.1551-2916.2008.02601.x.

[39] S. El-Sayed, Thermal decomposition, kinetics and combustion parameters determination for two different sizes of rice husk using TGA, Eng. Agric. Environ. Food. 12 (4) (2019) 460–469, https://doi.org/10.1016/j.eaef.2019.08.002.

[40] R. Maddalena, C. Hall, A. Hamilton, Effect of silica particle size on the formation of calcium silicate hydrate [CSH] using thermal analysis, Thermochim. Acta 672 (2019) 142–149, https://doi.org/10.1016/j.tca.2018.09.003.

[41] E.T. Rodriguez, K. Garbev, D. Merz, L. Black, I.G. Richardson, Thermal stability of CSH phases and applicability of Richardson and Groves' and Richardson C-(A)-SH (I) models to synthetic CSH, Cement Concr. Res. 93 (2017) 45–56, https://doi.org/10.1016/j.cemconres.2016.12.005.

[42] Y. Ahn, S.-Y. Kwak, Functional mesoporous silica with controlled pore size for selective adsorption of free fatty acid and chlorophyll, Microporous Mesoporous Mater. 306 (2020) 110410, https://doi.org/10.1016/j.micromeso.2020.110410.

[43] W. Liao, H. Wang, Q. Cai, P. Yang, H.-q. Li, Enhanced Cu (II) removal performance and mechanisms on Fe (II)-Modified LDH-GO composites, Environ. Eng. Sci. 37 (11) (2020) 746–756, https://doi.org/10.1089/ees.2020.0094.

[44] M.R. Awual, M.M. Hasan, A. Islam, M.M. Rahman, A.M. Asiri, M.A. Khaleque, M.C. Sheikh, Introducing an amine functionalized novel conjugate material for toxic nitrite detection and adsorption from wastewater, J. Clean. Prod. 228 (2019) 778–785, https://doi.org/10.1016/j.jclepro.2019.04.280.

[45] Y. Zhang, R. Zheng, J. Zhao, F. Ma, Y. Zhang, Q. Meng, Characterization of-treated rice husk adsorbent and adsorption of copper (II) from aqueous solution, BioMed Res. Int. 2014 (2014) 1–8, https://doi.org/10.1155/2014/496878.

[46] D.W. Stephan, G. Erker, Frustrated Lewis pairs: metal-free hydrogen activation and more, Angew. Chem., Int. Ed. Engl. 49 (1) (2010) 46–76, https://doi.org/10.1002/anie.200903708.

[47] A. Vávra, M. Hájek, F. Skopal, The removal of free fatty acids from methyl ester, Renew. Energy 103 (2017) 695–700, https://doi.org/10.1016/j.renene.2016.10.084.

[48] C.C. Timbo, M. Kandawa-Schulz, M. Amuanyena, H.M. Kwaambwa, Adsorptive removal from aqueous solution of Cr (VI) by green moringa tea leaves biomass, J. Encapsulation Adsorpt. Sci. 7 (2) (2017) 108–119, https://doi.org/10.4236/jeas.2017.72008.

[49] F. Gorzin, M. Bahri Rasht Abadi, Adsorption of Cr (VI) from aqueous solution by adsorbent prepared from paper mill sludge: kinetics and thermodynamics studies, Adsorpt. Sci. Technol. 36 (1–2) (2018) 149–169, https://doi.org/10.1177/0263617416686976.

[50] A.I. Rehan, A.I. Rasee, M.E. Awual, R.M. Waliullah, M.S. Hossain, K.T. Kubra, M.S. Salman, M.M. Hasan, M.N. Hasan, M.C. Sheikh, H.M. Marwani, M.A. Khaleque, A. Islam, M.R. Awual, Improving toxic dye removal and remediation using novel nanocomposite fibrous adsorbent, Colloids Surf. A Physicochem. Eng. Asp. 673 (2023) 131859, https://doi.org/10.1016/j.colsurfa.2023.131859.

[51] H. Radnia, A.A. Ghoreyshi, H. Younesi, G.D. Najafpour, Adsorption of Fe (II) ions from aqueous phase by chitosan adsorbent: equilibrium, kinetic, and thermodynamic studies, Desalination Water Treat. 50 (1–3) (2012) 348–359, https://doi.org/10.1080/19443994.2012.720112.

[52] T. Ma, Y. Wu, N. Liu, Y. Wu, Hydrolyzed polyacrylamide modified diatomite waste as a novel adsorbent for organic dye removal: adsorption performance and mechanism studies, Polyhedron 175 (2020) 114227, https://doi.org/10.1016/j.poly.2019.114227.

[53] A.I. Rasee, E. Awual, A.I. Rehan, M.S. Hossain, R.M. Waliullah, K.T. Kubra, M.C. Sheikh, M.S. Salman, M.N. Hasan, M.M. Hasan, H.M. Marwani, A. Islam, M.A. Khaleque, M.R. Awual, Efficient separation, adsorption, and recovery of Samarium(III) ions using novel ligand-based composite adsorbent, Surface. Interfac. 41 (2023) 103276, https://doi.org/10.1016/j.surfin.2023.103276.

[54] M.S. Salman, M.C. Sheikh, M.M. Hasan, M.N. Hasan, K.T. Kubra, A.I. Rehan, M.E. Awual, A.I. Rasee, R.M. Waliullah, M.S. Hossain, M.A. Khaleque, A.K.D. Alsukaibi, H.M. Alshammari, M.R. Awual, Chitosan-coated cotton fiber composite for efficient toxic dye encapsulation from aqueous media, Appl. Surf. Sci. 622 (2023) 157008, https://doi.org/10.1016/j.apsusc.2023.157008.

[55] S. Banerjee, M. Chattopadhyaya, Adsorption characteristics for the removal of a toxic dye, tartrazine from aqueous solutions by a low cost agricultural by-product, Arab. J. Chem. 10 (2017) S1629–S1638, https://doi.org/10.1016/j.arabjc.2013.06.005.

[56] L. Dhar, S. Hossain, M.S. Rahman, S.B. Quraishi, K. Saha, F. Rahman, M.T. Rahman, Adsorption mechanism of methylene blue by graphene oxide-shielded Mg–Al-layered double hydroxide from synthetic wastewater, J. Phys. Chem. A 125 (4) (2021) 954–965, https://doi.org/10.1021/acs.jpca.0c09124.

[57] D.L. Wilson, S. Zaccheus, F.F. Yirankinyuki, P.S. Kwarson, Temperature effects and thermodynamic adsorption of flouride on activated coconut shell carbon, activated montmorillonite clay and rice husk ash, Adv. Res. Chem. Sci. 4 (9) (2017) 21–27, https://doi.org/10.20431/2349-0403.0409003.

[58] L. Bo, F. Gao, Y. Bian, Z. Liu, Y. Dai, A novel adsorbent Auricularia Auricular for the removal of methylene blue from aqueous solution: isotherm and kinetics studies, Environ. Technol. Innov. 23 (2021) 101576, https://doi.org/10.1016/j.eti.2021.101576.

[59] L. Zeng, L. Yang, S. Wang, K. Yang, Synthesis and characterization of different crystalline calcium silicate hydrate: application for the removal of aflatoxin B1 from aqueous solution, J. Nanomater. 2014 (2014) 1–10, https://doi.org/10.1155/2014/431925.

[60] M. Kumar, H.S. Dosanjh, H. Singh, Magnetic zinc ferrite–chitosan bio-composite: synthesis, characterization and adsorption behavior studies for cationic dyes in single and binary systems, J. Inorg. Organomet. Polym. Mater. 28 (3) (2018) 880–898, https://doi.org/10.1007/s10904-017-0752-0.

[61] M. Toor, B. Jin, Adsorption characteristics, isotherm, kinetics, and diffusion of modified natural bentonite for removing diazo dye, Chem. Eng. J. 187 (2012) 79–88, https://doi.org/10.1016/j.cej.2012.01.089.

[62] M.A. Hubbe, S. Azizian, S. Douven, Implications of apparent pseudo-second-order adsorption kinetics onto cellulosic materials: a review, Bioresources 14 (3) (2019) 7582–7626, https://doi.org/10.15376/biores.14.3.7582-7626.

[63] U. Mahapatra, A.K. Manna, A. Chatterjee, A critical evaluation of conventional kinetic and isotherm modeling for adsorptive removal of hexavalent chromium and methylene blue by natural rubber sludge-derived activated carbon and commercial activated carbon, Bioresour. Technol. 343 (2022) 126135, https://doi.org/10.1016/j.biortech.2021.126135.

[64] M.R. Awual, I.M.M. Rahman, T. Yaita, M.A. Khaleque, M. Ferdows, pH dependent Cu(II) and Pd(II) ions detection and removal from aqueous media by an efficient mesoporous adsorbent, Chem. Eng. J. 236 (2014) 100–109, https://doi.org/10.1016/j.cej.2013.09.083.

[65] H. Wang, Y. Chen, Y. Wei, A novel magnetic calcium silicate/graphene oxide composite material for selective adsorption of acridine orange from aqueous solutions, RSC Adv. 6 (41) (2016) 34770–34781, https://doi.org/10.1039/C6RA07625D.

[66] S.K. Papageorgiou, E.P. Kouvelos, E.P. Favvas, A.A. Sapalidis, G.E. Romanos, F.K. Katsaros, Metal–carboxylate interactions in metal–alginate complexes studied with FTIR spectroscopy, Carbohydr. Res. 345 (4) (2010) 469–473, https://doi.org/10.1016/j.carres.2009.12.010.

[67] M.R. Awual, Efficient phosphate removal from water for controlling eutrophication using novel composite adsorbent, J. Clean. Prod. 228 (2019) 1311–1319, https://doi.org/10.1016/j.jclepro.2019.04.325.

[68] C. Zhang, Z. Wu, Z. Li, H. Li, J.-M. Lin, Inhibition effect of negative air ions on adsorption between volatile organic compounds and environmental particulate matter, Langmuir 36 (18) (2020) 5078–5083, https://doi.org/10.1021/acs.langmuir.0c00109.

[69] R. Jasrotia, J. Singh, S. Mittal, H. Singh, Synthesis of CTAB modified ferrite composite for the efficient removal of brilliant green dye, Int. J. Environ. Anal. Chem. (2022) 1–17, https://doi.org/10.1080/03067319.2022.2098485.

[70] M.C. Sheikh, M.M. Hasan, M.N. Hasan, M.S. Salman, K.T. Kubra, M.E. Awual, R.M. Waliullah, A.I. Rasee, A.I. Rehan, M.S. Hossain, H.M. Marwani, A. Islam, M.A. Khaleque, M.R. Awual, Toxic cadmium(II) monitoring and removal from aqueous solution using ligand-based facial composite adsorbent, J. Mol. Liq. 389 (2023) 122854, https://doi.org/10.1016/j.molliq.2023.122854.

[71] B. Baptiste, N. Esther, P. Mirela, K. Richard, Adsorption isotherm and kinetics modeling of carotene and free fatty acids adsorption from palm oil onto montmorillonite, Int. J. Biosci. 3 (3) (2013) 15–24, https://doi.org/10.12692/ijb/3.3.15-24.

[72] D. Sharma, R. Jasrotia, J. Singh, S. Mittal, H. Singh, Novel Zinc ferrite composite with starch and carboxy methyl starch from biowaste precursor for the removal of Ni (II) ion from aqueous solutions, J. Dispersion Sci. Technol. (2023) 1–11, https://doi.org/10.1080/01932691.2023.2222809.